Supporting Information

Versatile electrocatalytic processes realized by Ni, Co and Fe alloyed cores coordinated carbon shells

Xunyu Lu[1#,], Xin Tan[2#], Qingran Zhang[1], Rahman Daiyan[1], Jian Pan[1], Rui Chen[1], Hassan A. Tahini,[2] Da-Wei Wang[1], Sean C. Smith[2]*, Rose Amal[1]*

[1]Particles and Catalysis Research Group, School of Chemical Engineering, The University of New South Wales, Sydney, NSW 2052, Australia.
[2]Integrated Materials Design Laboratory, Research School of Physics and Engineering, The Australian National University, Canberra, ACT 2601, Australia.

[#] These authors contribute equally to this work.
*Email: r.amal@unsw.edu.au

sean.smith@anu.edu.au

Experimental details

Preparation of the M@C composites: Carbon black will be firstly stirred in 6 M HCl for 24 hours to remove any possible impurities. Then, 1.5 g of o-phenylenediamine (oPD, Sigma-Aldrich) will be dissolved in 25 mL of 1M HNO_3, followed by the addition of 0.2 g of carbon black and a certain amount of the corresponding metal precursors. The recipes for preparing all M@C composites in this study can be referred to Table S1. The reaction mixture is allowed to stir vigorously for ~ 10 min, and the solvent will be removed by rotating evaporation. The resultant powder will be ground, and pyrolyzed in a tube furnace at 900°C for 2.5 h, under an argon environment at a ramping rate of 3 ◦C min^{-1}. Finally, the composites will be stirred in 0.5 M H_2SO_4 solution at 90°C for 5 hours to remove the unwrapped metal components, and subjected to another pyrolysis treatment at 900°C for 2.5 h under an argon environment at a ramping rate of 3◦C min^{-1}. Unless specifically mentioned, all samples prepared in this study were pyrolyzed under the same temperature of 900°C.

Preparation of NiCoFe@C-800: The NiCoFe@C-800 composite was prepared according to the method mentioned above, with the only exception of being pyrolyzed at 800 °C for two times.

Preparation of NC: The NC background was synthesized according to the method to prepared M@C composites in the absence of metal precursors.

Physical and Chemical Characterization: XPS was performed on a Thermo ESCALAB250i X-ray Photoelectron Spectrometer. TEM was performed using a Philips CM 200 microscope. XRD was performed on a PANalytical X'Pert instrument. Raman spectroscopy was carried out on a Renishaw inVia Raman Microscope using the 514 nm laser. STEM was performed using a JEOL JEM-ARM200F microscope.

Electrochemical Characterization: All electrochemical measurements were carried out with a CHI 750E electrochemical workstation (CH Instrument). First of all, the obtained M@C composites, NC background, Ir/C (20 wt% of Ir, FuelCellStore) and Pt/C (20 wt% of Pt, Sigma-Aldrich) were prepared into catalyst inks before drop-casting onto glassy carbon (GC) work electrodes. Specifically, 5 mg of the powder sample was added into 1 mL of water and ethanol solution (1:1, v/v), followed by the addition of 25 μL of Nafion 117 solution (Sigma-Aldrich). The mixture was then sonicated for at least 20 min to form a homogenous ink. The ink was then drop-casted onto GC substrates to achieve a loading of 0.8 mg cm^{-2} for M@C and NC composites, and a loading of 0.2 mg cm^{-2} for Ir/C and Pt/C. All electrochemical measurements were carried out in a customized cell, employing the catalyst loaded GC as the working electrode, a Pt wire as the counter electrode and a SCE electrode as the reference. 1 M KOH aqueous solution was employed as the electrolyte in this study. All measured potentials were calibrated to RHE using the following equation: E_{RHE} (V) = E_{SCE} (V) + 0.245 + 0.059 × pH. OER and HER polarization curves were recorded at a scan rate of 5 mV s^{-1}. The ORR polarization curves were obtained with catalyst drop-casted GC rotating disk electrode (RDE) in O_2 saturated 1 M KOH at 1600 rpm with a scan rate of 5 mV s^{-1}. Rotating ring disc electrode (RRDE) measurements were carried out with a Pt ring glassy carbon disc electrode (ALS Co.

Ltd). The catalyst inks were loaded onto the GC disc to achieve the same loading as on GC RDE. RRDE voltammetirc measurements were also carried out in O_2 saturated 1 M KOH at 1600 rpm with a scan rate of 5 mV s^{-1}. More details of RRDE measurement can be referred to Figure S4. The potential of the Pt ring was set at 1.2 V to detect the hydrogen peroxide produced on the disc. In this study, all electrochemical measurements were carried out without compensating the *i*R drop. The current densities mentioned herein were obtained based on geometric surface area.

Theoretical calculations: Our spin-polarized DFT calculations were performed using the Vienna Ab-initio Simulation Package (VASP) with the projector augmented wave method[1] and a cutoff energy of 400 eV. The generalized gradient approximation of Perdew, Burke, and Ernzerhof (GGA–PBE)[2] with van der Waals (vdW) correction proposed by Grimme (DFT-D2)[3] was used in all the calculations due to its good description of long-range vdW interactions. The models of metal particles encapsulated into graphene layer (M@Cs) consist of C_{240} encapsulating 55 atoms metal cluster,[4,5] such as Fe, Co, Ni and their alloys with the molar ratio Fe:Co:Ni=7:24:24, which is close to the composites used in our experiments. In geometry optimizations, all the atomic coordinates were fully relaxed up to the residual atomic forces smaller than 0.07 eV/Å, and the total energy was converged to 10^{-4} eV.

The overall HER mechanism is evaluated with a three-state diagram consisting of an initial H^+ state, an intermediate H* state, and 1/2 H_2 as the final product. The free energy of H* (ΔG_{H^*}) is proven to be a key descriptor to characterize the HER activity of the electrocatalyst. A electrocatalyst with a positive value leads to low kinetics of adsorption of hydrogen, while a catalyst with a negative value leads to low kinetics of release of hydrogen molecule.[6] The optimum value of $|\Delta G_{H^*}|$ should be zero; for instance, this value for the well-known highly efficient Pt catalyst is near-zero as $|\Delta G_{H^*}| \approx 0.09$ eV.[6] The ΔG_{H^*} is calculated as[7]

$$\Delta G_{H^*} = \Delta E_{H^*} + \Delta E_{ZPE} - T\Delta S_H \quad (1)$$

where ΔE_{H^*} is the binding energy of adsorbed hydrogen, and ΔE_{ZPE} and ΔS_H are the difference in zero point energy and entropy between the adsorbed hydrogen and hydrogen in the gas phase, respectively. As the contribution from the vibrational entropy of hydrogen in the adsorbed state is negligibly small, the entropy of hydrogen adsorption is $\Delta S_H \approx -\frac{1}{2} S_{H_2}$, where S_{H_2} is the entropy of H_2 in the gas phase at the standard conditions. Therefore, Eq. (1) can be rewritten as[7]

$$\Delta G_{H^*} = \Delta E_{H^*} + 0.37\text{eV} \quad (2)$$

It is well known that ORR process has two possible reaction pathways: two-electron transfer and four-electron transfer processes. Previous studies have shown that the four-electron reaction is much more efficient than the two-electron one for carbon-based electrocatalysts.[8] In alkaline media, the four-electron reaction mechanism follows several elementary steps:[8]

$$O_2(g) + * \rightarrow O_2^* \quad (3)$$

$$O_2^* + H_2O(l) + e^- \rightarrow OOH^* + OH^- \quad (4)$$

$$OOH^* + e^- \rightarrow O^* + OH^- \quad (5)$$

$$O^* + H_2O(l) + e^- \rightarrow OH^* + OH^- \quad (6)$$

$$OH^* + e^- \rightarrow OH^- + * \quad (7)$$

where the $*$ represents the active site on the electrocatalyst surface, (l) and (g) refer to liquid and gas phases, respectively, and O^*, OH^* and OOH^* are adsorbed intermediates.

As the OER is the reverse process of the ORR, the overall OER in alkaline media can be written as:[9]

$$OH^- + * \rightarrow OH^* + e^- \quad (8)$$

$$OH^* + OH^- \rightarrow O^* + H_2O(l) + e^- \quad (9)$$

$$O^* + OH^- \rightarrow OOH^* + e^- \quad (10)$$

$$OOH^* + OH^- \rightarrow O_2^* + H_2O(l) + e^- \quad (11)$$

$$O_2^* \rightarrow O_2(g) + * \quad (12)$$

Here, we took reactions (3)-(7) and reactions (8)-(12) to derive the thermochemistry for ORR and OER in alkaline media, respectively, and the overpotentials of ORR/OER processes can be determined by calculating the reaction free energies of the different elementary steps. By using DFT calculations in conjunction with standard hydrogen electrode (SHE) model developed by Nørskov and co-workers,[10,11] we can calculate the overpotential and determine the rate limiting step of OER/ORR for different catalysts.

The binding energies of OH^*, O^*, and OOH^* were obtained by DFT calculations as follows,[10,11]

$$\Delta E_{OH^*} = E(OH^*) - E(*) - (E_{H_2O} - 1/2E_{H_2}) \quad (13)$$

$$\Delta E_{OOH^*} = E(OOH^*) - E(*) - (2E_{H_2O} - 3/2E_{H_2}) \quad (14)$$

$$\Delta E_{O^*} = E(O^*) - E(*) - (E_{H_2O} - E_{H_2}) \quad (15)$$

in which, $E(*)$, $E(OH^*)$, $E(O^*)$, and $E(OOH^*)$ are the ground state energies of a clean surface and surfaces adsorbed with OH^*, O^*, and OOH^*, respectively. E_{H_2O} and E_{H_2} are the calculated DFT energies of H_2O and H_2 molecules in the gas phase. If we considered the ZPE and entropy correction, the free energies of adsorption, ΔG_{ads}, can be transformed from DFT binding energies, ΔE_{ads}, as follows:

$$\Delta G_{ads} = \Delta E_{ads} + \Delta ZPE - T\Delta S + eU \quad (16)$$

where ΔE_{ads} is the binding energy of adsorption species OH^*, O^*, and OOH^*. ΔZPE, ΔS, U and e are the ZPE changes, entropy changes, applied potential at the electrode, and charge transferred. The contributions of each component for ΔG_{ads} were obtained from previous literature, [12] and were listed in Table S2.

Using the adsorption free energies obtained from (16) and (13)-(15), the reaction free energies of ORR reactions (3)-(7) and OER reactions (8)-(12) can be calculated. For the ORR reactions,[10]

$$\Delta G_1 = \Delta G_{OOH^*} - 4.92 \quad (17)$$

$$\Delta G_2 = \Delta G_{O^*} - \Delta G_{OOH^*} \quad (18)$$

$$\Delta G_3 = \Delta G_{OH^*} - \Delta G_{O^*} \quad (19)$$

$$\Delta G_4 = -\Delta G_{OH^*} \quad (20)$$

And for the OER reactions,[11]

$$\Delta G_1 = \Delta G_{OH^*} \quad (21)$$

$$\Delta G_2 = \Delta G_{O^*} - \Delta G_{OH^*} \quad (22)$$

$$\Delta G_3 = \Delta G_{OOH^*} - \Delta G_{O^*} \quad (23)$$

$$\Delta G_4 = 4.92 - \Delta G_{OOH^*} \quad (24)$$

Thus, for the ORR reactions, the overpotential, η^{ORR}, can be expressed as:[10]

$$G^{ORR} = \max\{\Delta G_1, \Delta G_2, \Delta G_3, \Delta G_4\} \quad (25)$$

$$\eta^{ORR} = 1.23\ V - \left|G^{ORR}\right|/e \quad (26)$$

where ΔG_1, ΔG_2, ΔG_3, and ΔG_4 are the free energy of reactions (3)-(7), respectively. And for OER reactions, the overpotential, η^{OER}, can be expressed as:[11]

$$G^{OER} = \max\{\Delta G_1, \Delta G_2, \Delta G_3, \Delta G_4\} \quad (27)$$

$$\eta^{OER} = \left|G^{OER}\right|/e - 1.23\ V \quad (28)$$

where ΔG_1, ΔG_2, ΔG_3, and ΔG_4 are the free energy of reactions (8)-(12), respectively.

Table S1. Recipes for the preparation of M@C composites.

Name	$Ni(NO_3)_2$	$Co(NO_3)_2$	$Fe(NO_3)_3$	oPD	CB
Ni@C	2.6 mmol	0	0	1.5g	0.2 g
Co@C	0	2.6 mmol	0	1.5g	0.2 g
Fe@C	0	0	2.6 mmol	1.5g	0.2 g
NiCo@C	1.3 mmol	1.3 mmol	0	1.5g	0.2 g
NiFe@C	1.8 mmol	0	0.8 mmol	1.5g	0.2 g
CoFe@C	1.8 mmol	0	0.8 mmol	1.5g	0.2 g
NiCoFe@C	1.13 mmol	1.13 mmol	0.34 mmol	1.5g	0.2 g
2/3 NiCoFe@C	0.75 mmol	0.75 mmol	0.22 mmol	1.5g	0.2 g

Table S2. Zero point energies and entropies of intermediates.

Intermediate	ZPE	Entropy
OOH*	0.475	0.000210
O*	0.088	0.000067
OH*	0.393	0.000091
H_2O	0.574	0.001957
H_2	0.351	0.001354

Table S3. Electrocatalytic OER activities of different recently reported materials.

Catalyst	$E_{j10,\ OER}$ (V)	Loading of Catalyst (mg cm^{-2})	Reference
Pt/C	1.85	0.26	[13]
Ir/C (20 wt%)	1.61	N/A	[14]
Ru/C (20 wt%)	1.62	N/A	[14]
Pt/C to BSCF/C = 4:1	1.61	0.26	[13]
Fe_3C@NG800-0.2	1.59	0.20	[15]
Co/N-C-800	1.60	0.25	[16]
CoS_2(400)N,S-GO	1.61	0.25	[17]
Fe/C/N	1.59	0.20	[18]
N-graphene/CNT	1.65	0.88	[19]
Hierarchical nanostructured $NiCo_2O_4$	1.62	N/A	[20]
SN-Fe_{27}	1.78	0.80	[21]
3D mesoporous graphene	1.56	0.60	[22]
CNT@NCNT	1.76	0.25	[23]
NiCoFe@C	**1.58 (j = 15 mA cm^{-2})**	**0.8**	**This work**

Table S4. Electrocatalytic ORR activities of different recently reported materials.

Samples	Catalysts Loading (mg cm^{-2})	*Onset potential (V vs RHE)*[a)]	*Half-wave potential (V vs RHE)*[a)]	Ref.
MnNPC-900	0.25	0.95	0.82	[24]
FePC	0.04	0.95	~ 0.78	[25]
CNTs-Co/NC	0.04	0.96	0.84	[26]
Co/N-CNTs	0.20	0.94	0.84	[27]
Co-N-C-900	0.20	0.972	0.905	[28]
Fe/P/C nanowire networks	0.46	0.884	0.815	[29]
Co-P,N-CNT	0.10	0.981	0.811	[30]
Fe©N-C-12	0.311	~ 0.93	~ 0.81	[31]
Fe/N-CNT	~ 0.20	~ 0.96	0.81	[32]
Fe_xP/NPCS	0.16	0.918	0.832	[33]
FeGH-$ArNH_3$	0.30	0.94	0.85	[34]
Fe,N-doped carbon	0.60	0.98	0.85	[35]
NiCoFe@C	**0.8**	**0.93**	**0.85**	**This work**

[a)] The ORR data was obtained over the catalysts in 0.1 M O_2-saturated KOH solution at a rotation speed of 1600 rpm.

Table S5. Electrocatalytic HER activities of different recently reported materials.

Catalyst	$E_{j10, HER}$ (V)	Loading of Catalyst (mg cm^{-2})	Reference
Ir/C (20 wt%)	-0.34	N/A	[13]
Ru/C (20 wt%)	-0.29	N/A	[13]
CoNi@NC	-0.224	0.32	[36]
Co@Co-N-C	-0.314	N/A	[37]
N-Co@G	-0.265	0.285	[38]
S-600	-0.262	0.285	[39]
PPy/FeTCPP/Co	-0.24	0.3	[40]
DG	-0.17	0.283	[41]
CoN_x/C	-0.17	2	[42]
Ni@graphene	-0.24	0.36	[43]
FeCo	-0.211	0.32	[44]
NiCoFe@C	**-0.26**	**0.8**	**This work**

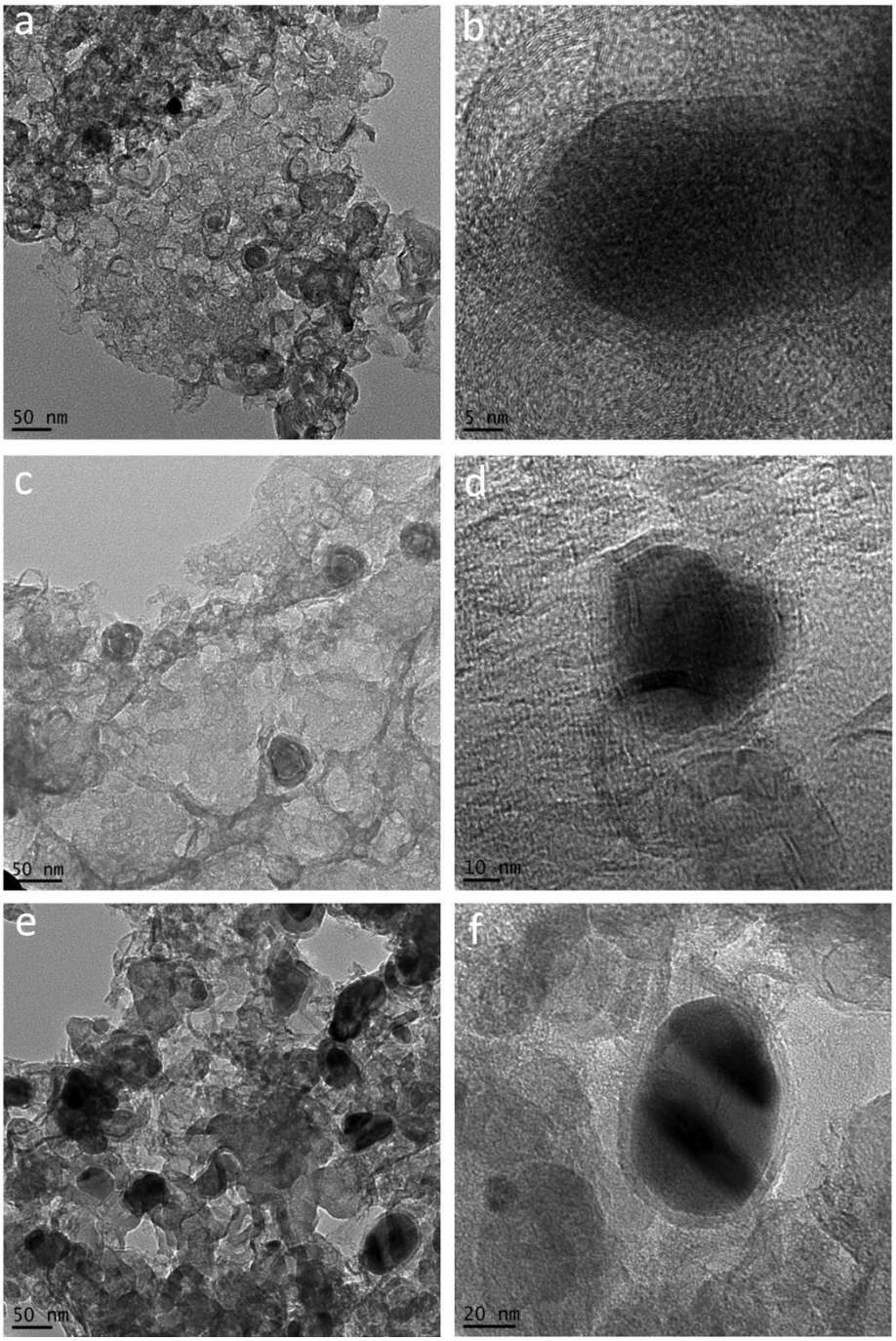

Figure S1. TEM images of **(a-b)** Fe@C, **(c-d)** Co@C and **(e-f)** NiFe@C composites.

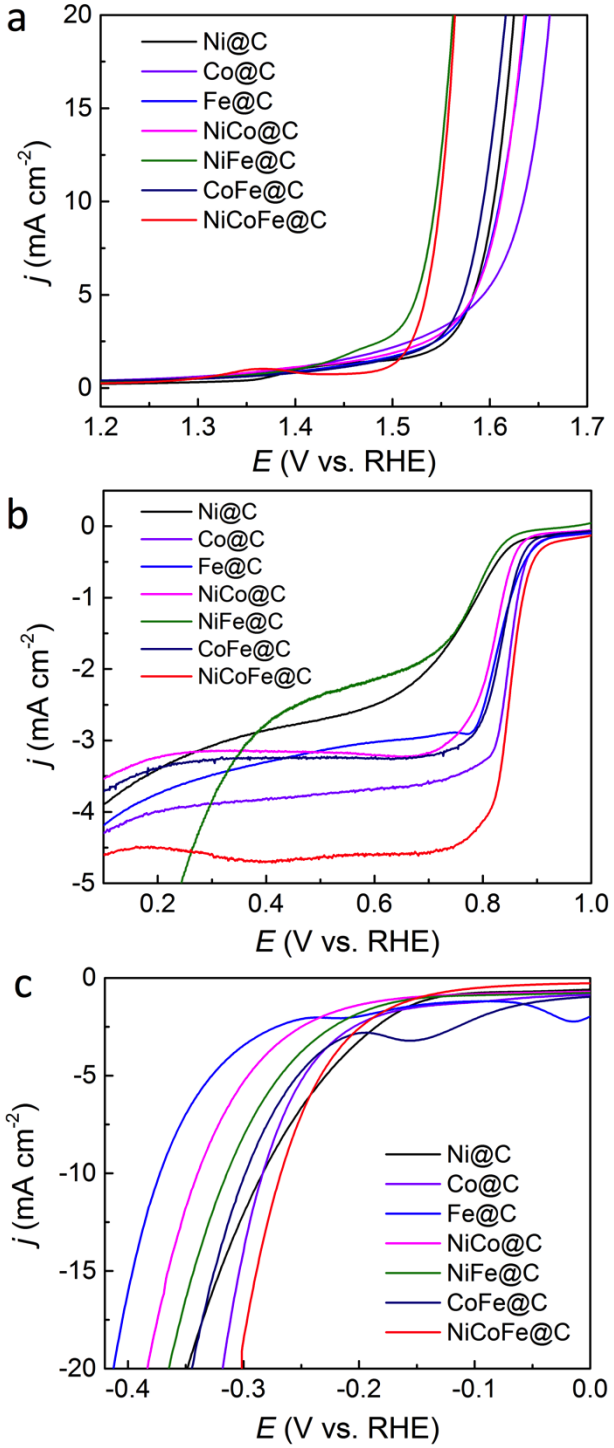

Figure S2. (a) OER polarization curves obtained with the M@C composites prepared in this study. **(b)** ORR polarization curves obtained with the M@C composites in O_2-sautrated 1 M

KOH at a 1600 rpm. **(c)** HER polarization curves obtained with the M@C composites. All reactions were carried out in 1 M KOH solution at a scan rate of 5 mV s^{-1}.

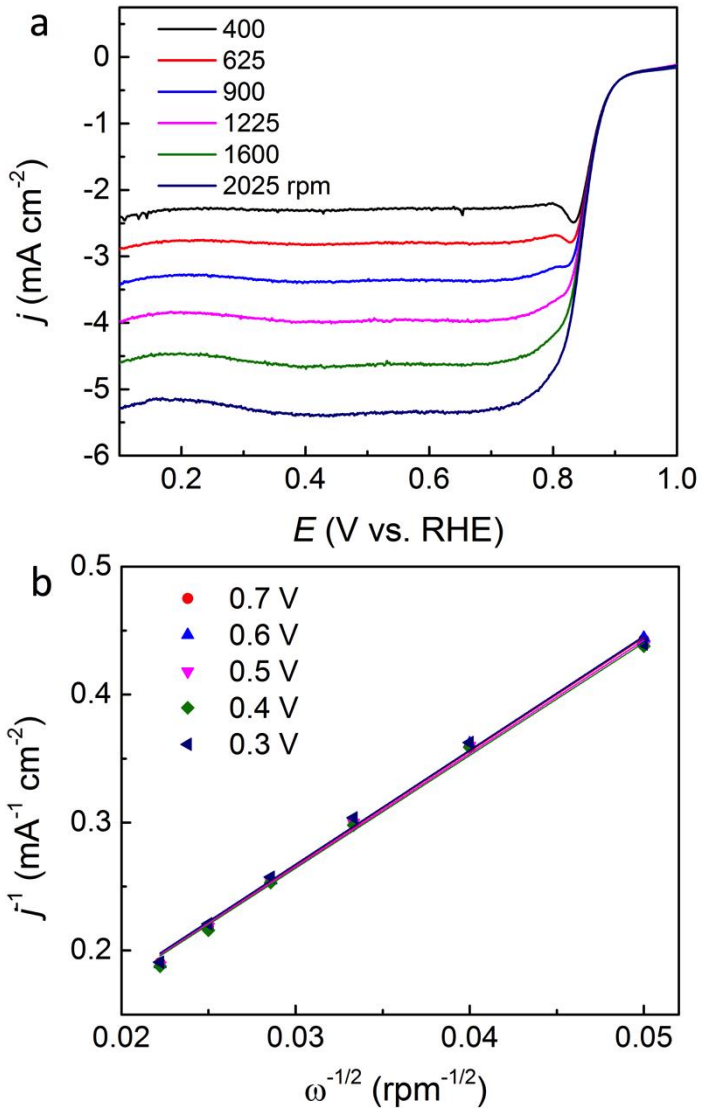

Figure S3. (a) RDE voltammogram obtained with NiCoFe@C drop-casted RDE in O_2-saturated 1 M KOH solution at various rotation rates. **(b)** Koutecky–Levich plots (current density^{-1} vs. rotating rate$^{-1/2}$) for NiCoFe@C drop-casted RDE at different potentials.

Figure S3 represents the rotating disc electrode (RDE) voltammograms obtained with NiCoFe@C modified glassy carbon (GC) electrode at different rotating rates. The oxygen reduction current density increases with the increase of rotating rates owing to enhanced mass transport. The Koutecky–Levich equation was applied to calculate the number of electrons (n)

transferred in ORR.[45,46] In a wide potential range of 0.3 V to 0.8 V, n is determined ~ 4, indicating a four-electron transfer pathway for ORR. The parallel and good linear fitting lines (Fig. S3b) demonstrate the first-order kinetics of NiCoFe@C catalyzed ORR in alkaline media.

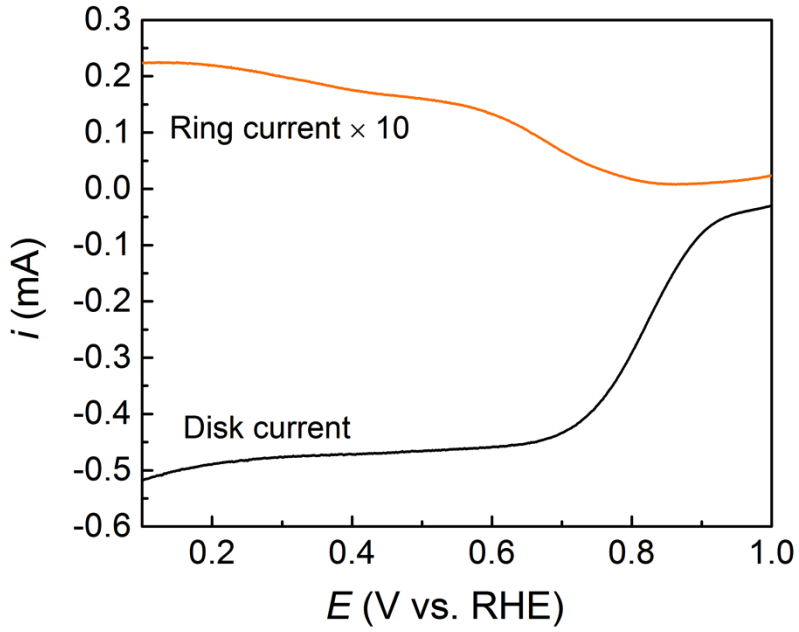

Figure S4. RRDE voltammetry of the NC background at the rotataing rate of 1600 rpm in O_2 saturated 1 M KOH with a scan rate of 5 mV s^{-1}.

RRDE measurement

The electron transfer number (n) per O_2 molecule involved in ORR and the percentage HO_2^- that has been generated during the ORR were calculated using the following equations:[47]

$$n = 4 \times \frac{I_D}{I_D + I_R / N}$$

$$HO_2^-\% = 200 \times \frac{I_R / N}{I_D + I_R / N}$$

Where I_D and I_R are the disk and ring currents, respectively. N is the collection efficiency, which is determined to be 0.3 in this study.

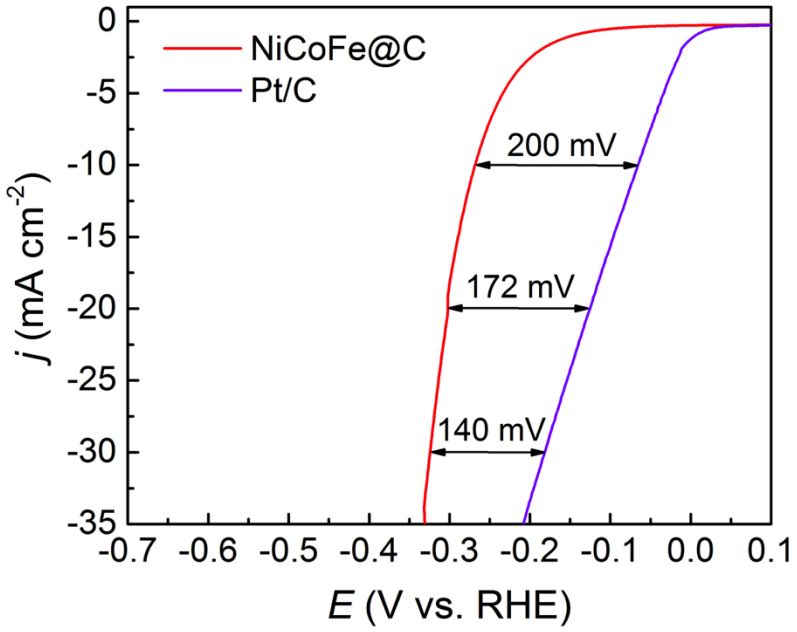

Figure S5. HER polarization curves obtained with NiCoFe@C and Pt/C drop-casted GC electrode in 1 M KOH with a scan rate of 5 mV s^{-1}.

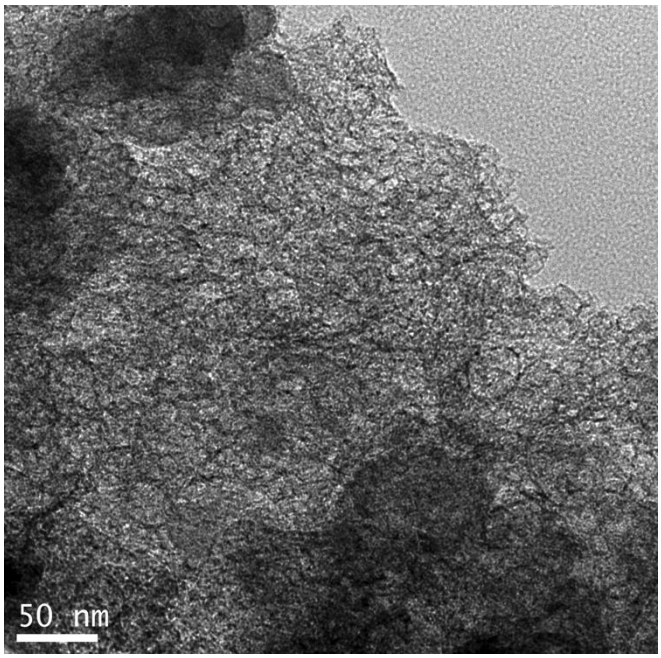

Figure S6. TEM image of the NiCoFe@C composite. It can be seen from this figure that the NiCoFe@C composite exhibited numerous pores on the carbon matrix, which may be formed owing to the polymerization and carbonization of the oPD precursor as well as the removal of imperfectly wrapped metal nanoparticles during acid treatments.

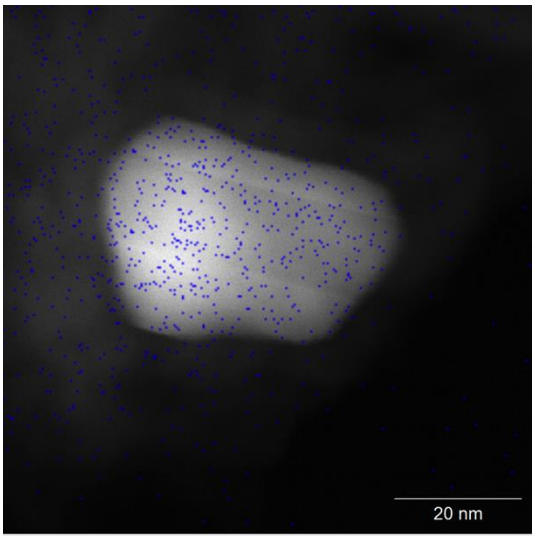

Figure S7. The O element mapping of the area indicated in Figure 3a.

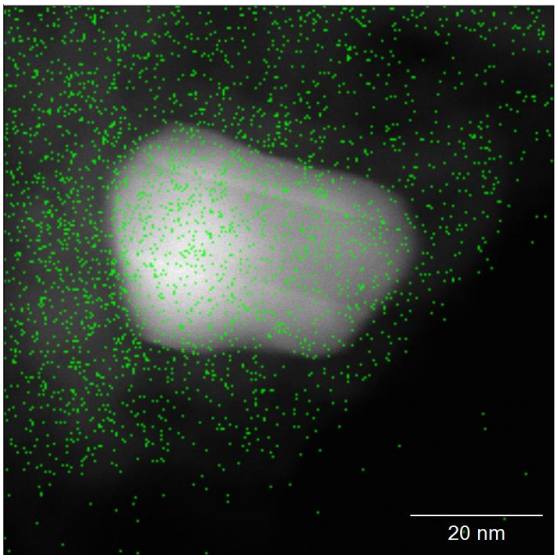

Figure S8. The N element mapping of the area indicated in Figure 3a.

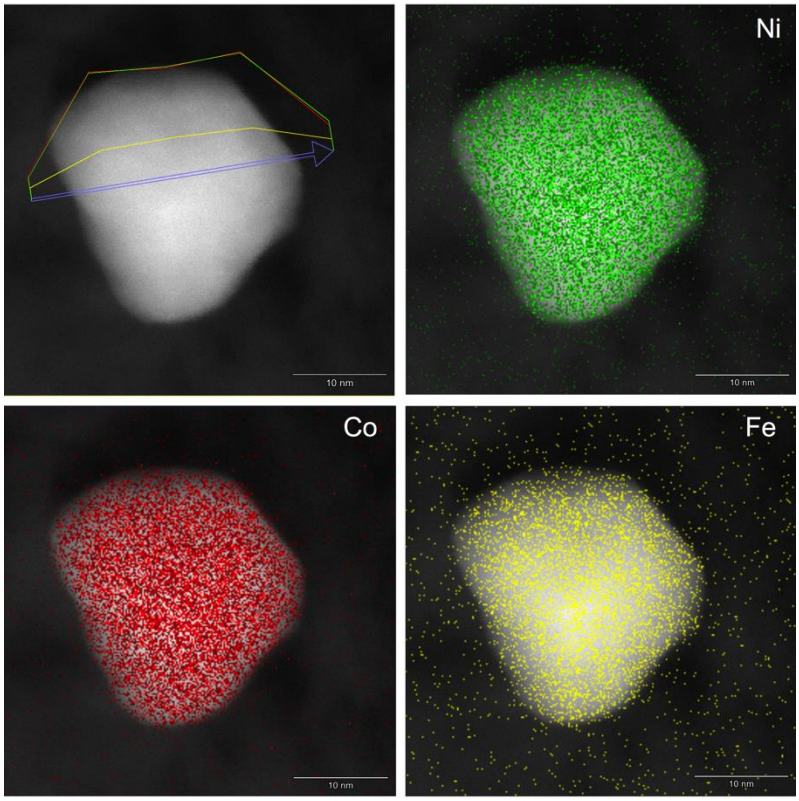

Figure S9. HADDF-STEM image and the corresponding elemental mappings of another NiCoFe alloyed nanoparticle in the NiCoFe@C composite.

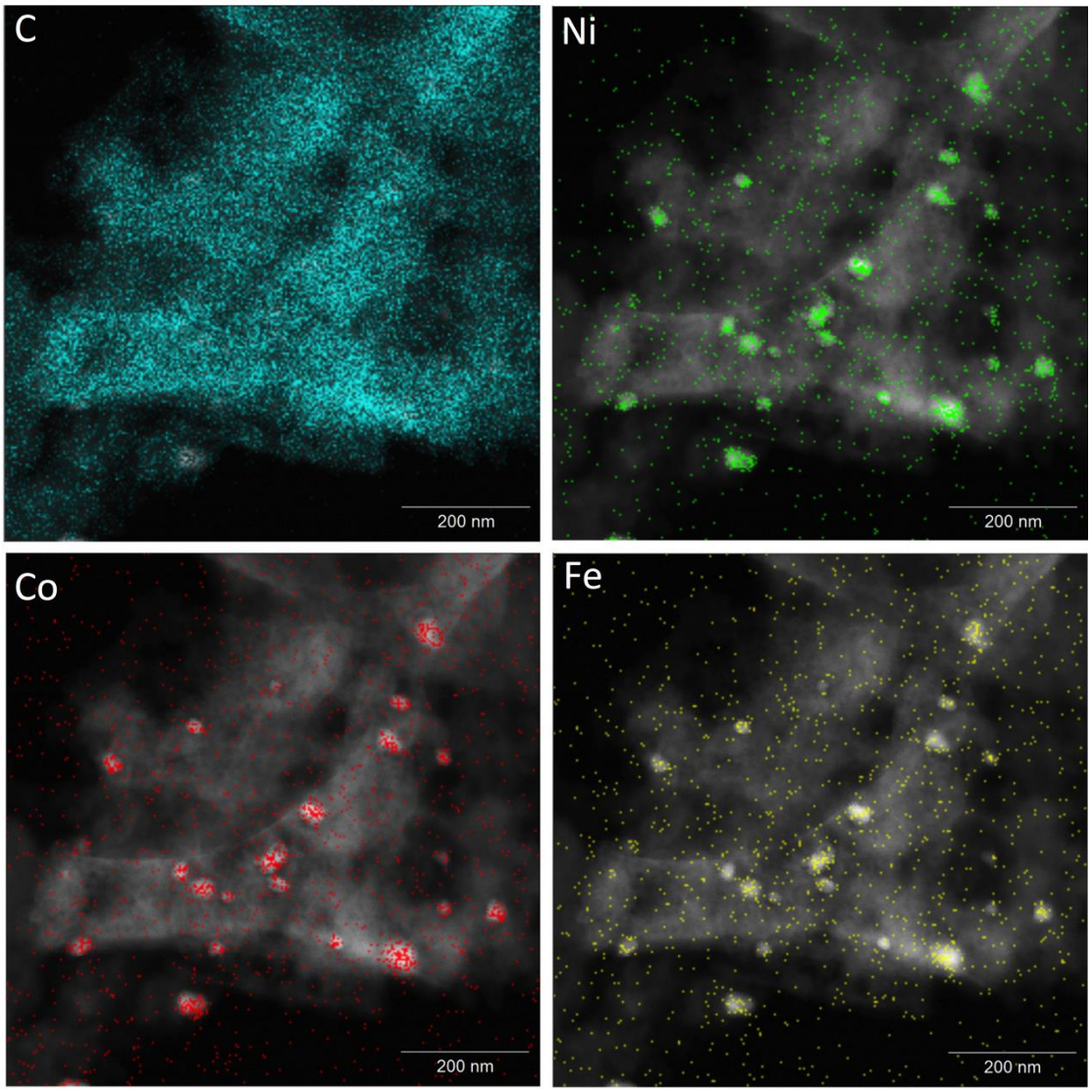

Figure S10. EDX analysis of the NiCoFe@C composite in a relatively large area.

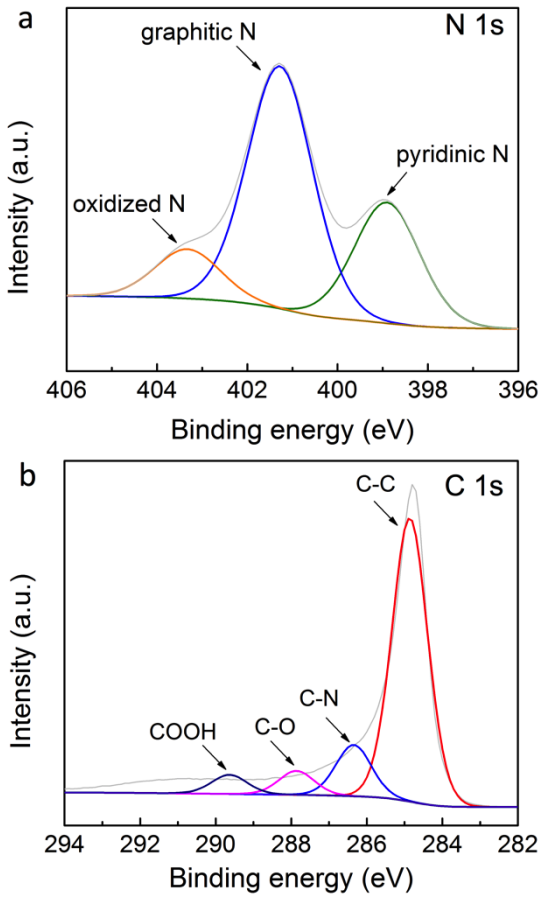

Figure S11. High-resolution **(a)** N 1s and **(b)** C 1s XPS survey spectra of the NiCoFe@C composite.

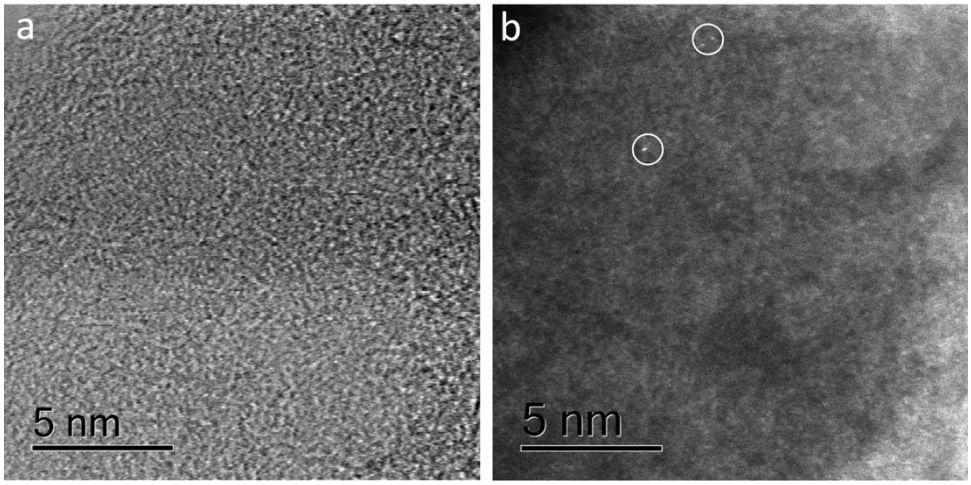

Figure S12. High resolution STEM **(a)** and HADDF-STEM **(b)** images of the carbon matrix in the NiCoFe@C composite. The bright spots circled in Figure S10b are belonging to Si impurities as determined by EELS measurement.

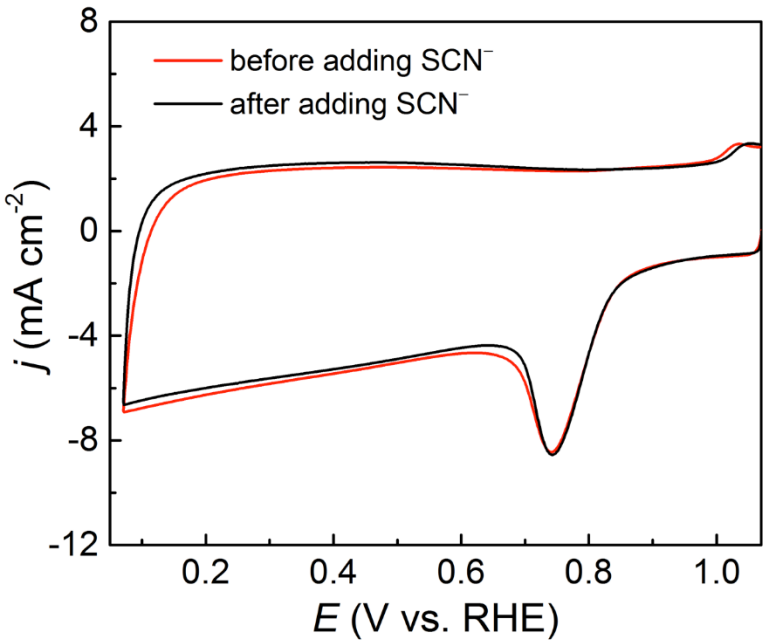

Figure S13. The poisoning effect on ORR in 1 M KOH with NiCoFe@C due to addition of 10 mM of KSCN. The polarization curves indicate that the ORR activity with the catalyst is not affected by the SCN^- ions.

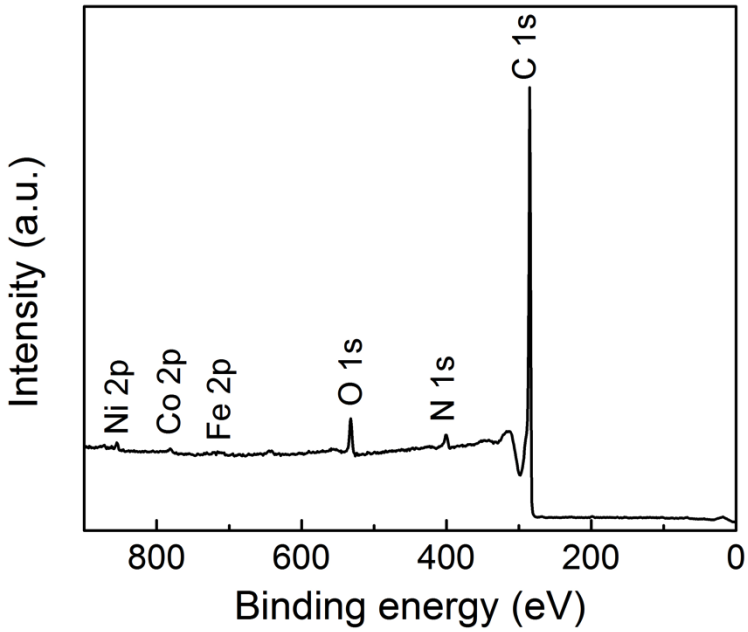

Figure S14. XPS survey spectrum of the NiCoFe@C-800 composite.

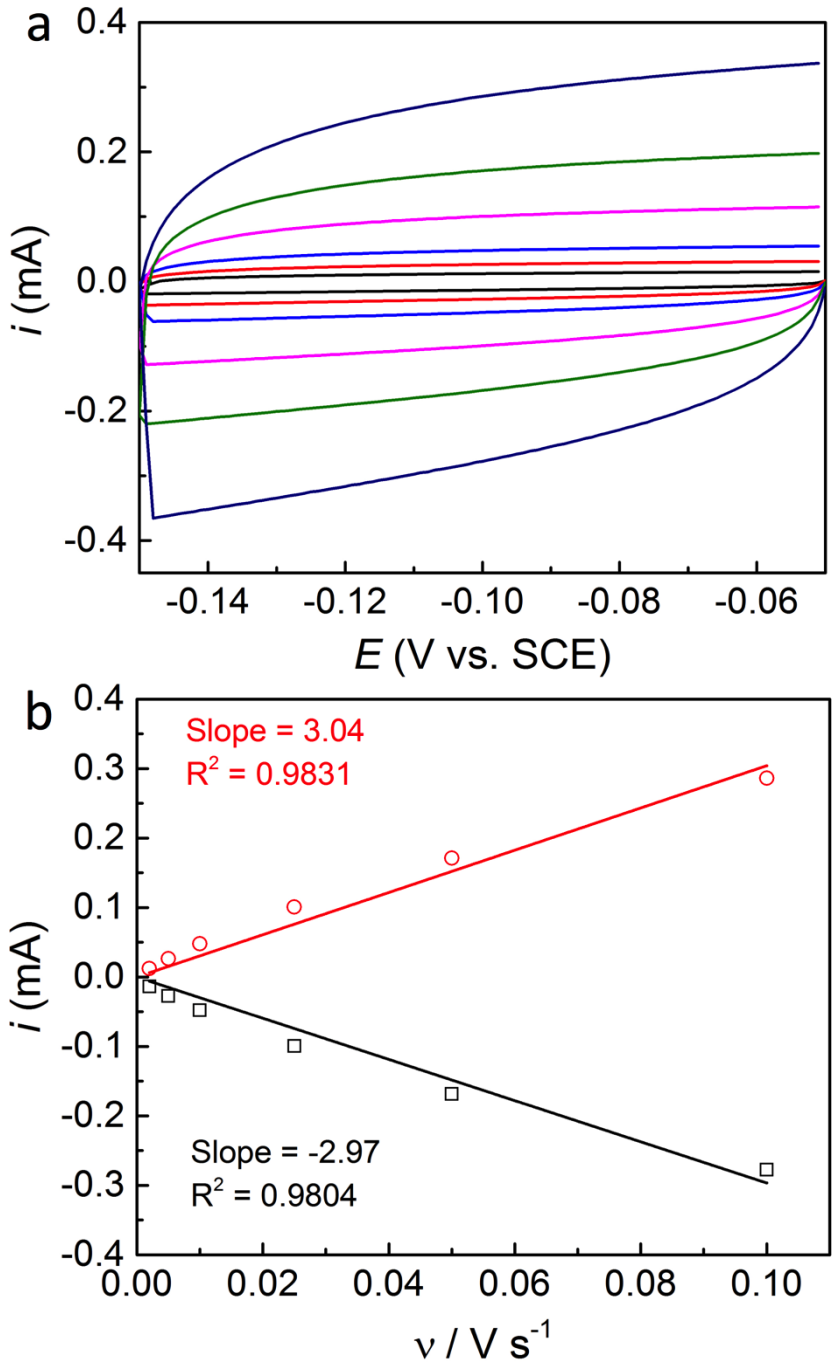

Figure S15. Electrochemical Surface Area (ECSA) measurements of NiCoFe@C-800 composite. **(a)** Cyclic voltammograms and **(b)** cathodic (black square) and anodic (red circle) capacitance currents measured at -0.1 V vs. SCE plotted as a function of scan rate of 2,5,10, 25, 50 and 100 mV s^{-1}, respectively. The double-layer capacitance determined from this system is taken from the average of the absolute value of anodic and cathodic slopes of the linear fits. The slope obtained with NiCoFe@C-800 composite is 3.005 mF/cm^2.

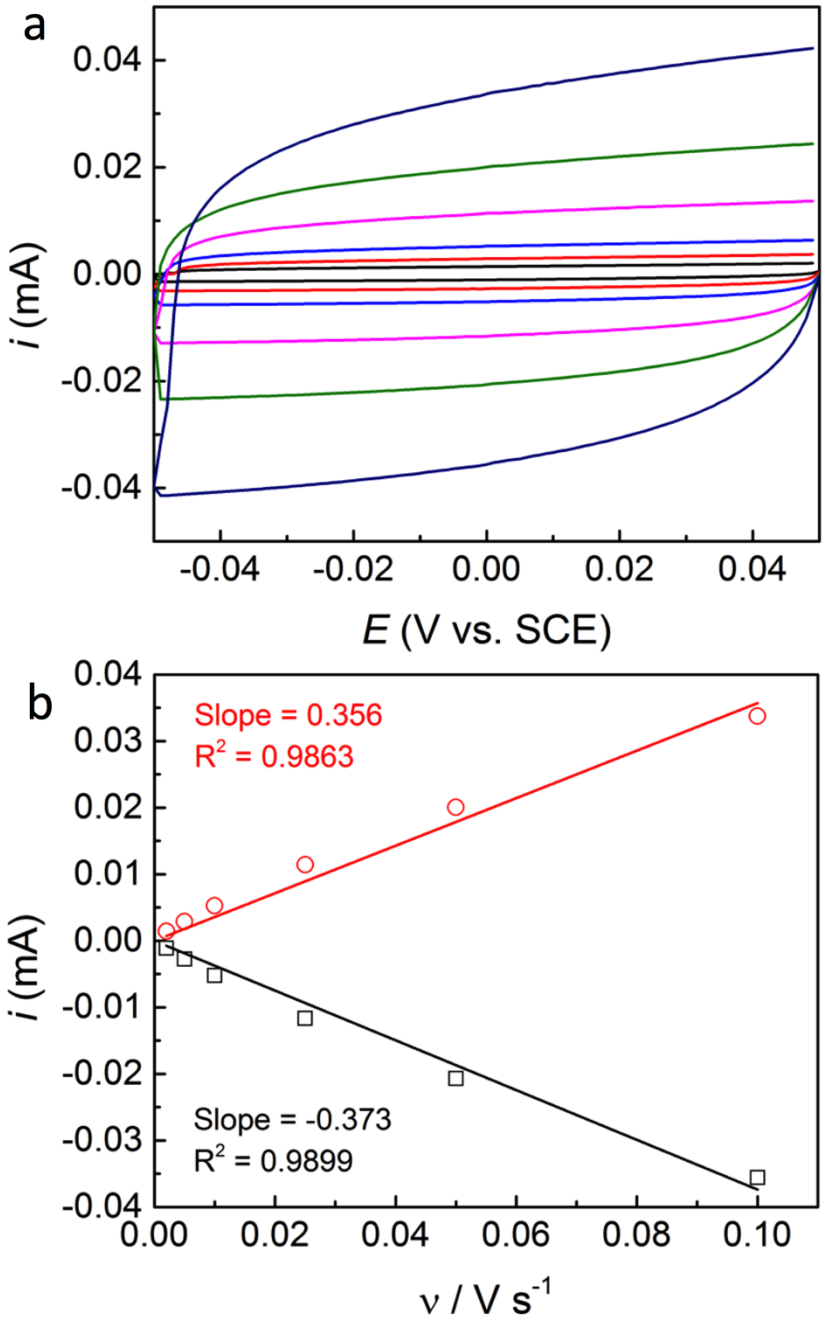

Figure S16. Electrochemical Surface Area (ECSA) measurements of NiCoFe@C-900 composite. **(a)** Cyclic voltammograms and **(b)** cathodic (black square) and anodic (red circle) capacitance currents measured at -0.1 V vs. SCE plotted as a function of scan rate of 2,5,10, 25, 50 and 100 mV s^{-1}, respectively. The double-layer capacitance determined from this system is taken from the average of the absolute value of anodic and cathodic slopes of the linear fits. The slope obtained with NiCoFe@C-900 composite is 0.3645 mF/cm^2.

References

(1) Kresse, G.; Joubert, D. From Ultrasoft Pseudopotentials to the Projector Augmented-Wave Method. *Phys. Rev. B* **1999**, *59*, 1758–1775.

(2) Perdew, J. P.; Burke, K.; Ernzerhof, M. Generalized Gradient Approximation Made Simple. *Phys. Rev. Lett.* **1996**, *77*, 3865–3868.

(3) Grimme, S. Semiempirical GGA-Type Density Functional Constructed with a Long-Range Dispersion Correction. *J. Comput. Chem.* **2006**, *27*, 1787–1799.

(4) Deng, J.; Ren, P.; Deng, D.; Bao, X. Enhanced Electron Penetration through an Ultrathin Graphene Layer for Highly Efficient Catalysis of the Hydrogen Evolution Reaction. *Angew. Chem. Int. Ed.* **2015**, *54*, 2100–2104.

(5) Cui, X.; Ren, P.; Deng, D.; Deng, J.; Bao, X. Single Layer Graphene Encapsulating Non-Precious Metals as High-Performance Electrocatalysts for Water Oxidation. *Energy Environ. Sci.* **2016**, *9*, 123–129.

(6) Nørskov, J. K.; Bligaard, T.; Logadottir, A.; Kitchin, J. R.; Chen, J. G.; Pandelov, S.; Stimming, U. Trends in the Exchange Current for Hydrogen Evolution. *J. Electrochem. Soc.* **2005**, *152*, J23–J26.

(7) Li, J.-S.; Wang, Y.; Liu, C.-H.; Li, S.-L.; Wang, Y.-G.; Dong, L.-Z.; Dai, Z.-H.; Li, Y.-F.; Lan, Y.-Q. Coupled Molybdenum Carbide and Reduced Graphene Oxide Electrocatalysts for Efficient Hydrogen Evolution. *Nat. Commun.* **2016**, *7*, 11204.

(8) Jiao, Y.; Zheng, Y.; Jaroniec, M.; Qiao, S. Z. Origin of the Electrocatalytic Oxygen Reduction Activity of Graphene-Based Catalysts: A Roadmap to Achieve the Best Performance. *J. Am. Chem. Soc.* **2014**, *136*, 4394–4403.

(9) Rossmeisl, J.; Logadottir, A.; Nørskov, J.K. Electrolysis of Water on (Oxidized) Metal Surfaces. *Chem. Phys.* **2005**, *319*, 178–184.

(10) Nørskov, J. K.; Rossmeisl, J.; Logadottir, A.; Lindqvist, L.; Kitchin, J. R.; Bligaard, T.;

Jónsson, H. Origin of the Overpotential for Oxygen Reduction at a Fuel-Cell Cathode. *J. Phys. Chem. B* **2004**, *108*, 17886–17892.

(11) Man, I. C.; Su, H.-Y.; Calle-Vallejo, F.; Hansen, H. A.; Martínez, J. I.; Inoglu, N. G.; Kitchin, J.; Jaramillo, T. F.; Nørskov, J. K.; Rossmeisl, J. Universality in Oxygen Evolution Electrocatalysis on Oxide Surfaces. *ChemCatChem* **2011**, *3*, 1159–1165.

(12) Studt, F. The Oxygen Reduction Reaction on Nitrogen-Doped Graphene. *Catal. Lett.* **2013**, *143*, 58–60.

(13) Y. Zhu, C. Su, X. Xu, W. Zhou, R. Ran, Z. Shao, *Chem. - A Eur. J.* **2014**, *20*, 13533.

(14) Y. Gorlin, T. F. Jaramillo, *J. Am. Chem. Soc.* **2010**, *132*, 13612.

(15) H. Jiang, Y. Yao, Y. Zhu, Y. Liu, Y. Su, X. Yang, C. Li, *ACS Appl. Mater. Interfaces* **2015**, *7*, 21511–21520.

(16) R. Singhal, V. Kalra, *ChemPhysChem* **2017**, *18*, 223.

(17) P. Ganesan, M. Prabu, J. Sanetuntikul, S. Shanmugam, *ACS Catal.* **2015**, *5*, 3625.

(18) Y. Zhao, K. Kamiya, K. Hashimoto, S. Nakanishi, *J. Phys. Chem. C* **2015**, *119*, 2583.

(19) Z. Wen, S. Ci, Y. Hou, J. Chen, *Angew. Chemie - Int. Ed.* **2014**, *53*, 6496.

(20) M. Prabu, K. Ketpang, S. Shanmugam, *Nanoscale* **2014**, *6*, 3173.

(21) N. R. Sahraie, J. P. Paraknowitsch, C. Go, A. Thomas, P. Strasser, *J. Am. Chem. Soc.* **2014**, *136*, 14486.

(22) K. J. Lee, Y. J. Sa, H. Y. Jeong, C. W. Bielawski, S. H. Joo, H. R. Moon, *Chem. Commun.* **2015**, *51*, 6773.

(23) G. L. Tian, Q. Zhang, B. Zhang, Y. G. Jin, J. Q. Huang, D. S. Su, F. Wei, *Adv. Funct. Mater.* **2014**, *24*, 5956.

(24) X. Zhu, R. Amal, X. Lu, *Small*, 2019, 1804524. DOI: 10.1002/smll.201804524.

(25) K. P. Singh, E. J. Bae and J. S. Yu, *J. Am. Chem. Soc.*, 2015, **137**, 3165.

(26) Y. Liu, H. Jiang, Y. Zhu, X. Yang, C. Li, *J. Mater. Chem. A* **2016**, *4*, 1694.

(27) S. Liu, I. S. Amiinu, X. Liu, J. Zhang, M. Bao, T. Meng, S. Mu, Chem. Eng.g J. 2018, 342, 163.

(28) C. Zhu, Q. Shi, B. Z. Xu, S. Fu, G. Wan, C. Yang, S. Yao, J. Song, H. Zhou, D. Du, S. P. Beckman, D. Su, Y. Lin, Adv. Energy Mater. DOI: 10.1002/aenm.201801956.

(29) M. Li, T. Liu, X. Bo, M. Zhou, L. Guo and S. Guo, *Nano Energy*, 2017, **33**, 221.

(30) S. Guo, P. Yuan, J. Zhang, P. Jin, H. Sun, K. Lei, X. Pang, Q. Xu and F. Cheng, *Chem. Commun.*, 2017, **53**, 9862.

(31) Y. Ye, H. Li, F. Cai, C. Yan, R. Si, S. Miao, Y. Li, G. Wang and X. Bao, ACS Catal., 2017, 7, 7638.

(32) Y. Liu, H. Jiang, Y. Zhu, X. Yang and C. Li, J. Mater. Chem. A, 2016, 4, 1694.

(33) K. Hu, Z. Xiao, Y. Cheng, D. Yan, R. Chen, J. Huo and S. Wang, Electrochim. Acta, 2017, 254, 280.

(34) M. Wang, Y. Yang, X. Liu, Z. Pu, Z. Kou, P. Zhu and S. Mu, Nanoscale, 2017, 9, 7641.

(35) Y. Wang, A. Kong, X. Chen, Q. Lin and P. Feng, ACS Catal., 2015, 5, 3887.

(36) J. Deng, P. Ren, D. Deng, X. Bao, *Angew. Chemie - Int. Ed.* **2015**, *54*, 2100.

(37) Y. Wang, Y. Nie, W. Ding, S. G. Chen, K. Xiong, X. Q. Qi, Y. Zhang, J. Wang, Z. D. Wei, *Chem. Commun.* **2015**, *51*, 8942.

(38) H. Fei, Y. Yang, Z. Peng, G. Ruan, Q. Zhong, L. Li, E. L. G. Samuel, J. M. Tour, *ACS Appl. Mater. Interfaces* **2015**, *7*, 8083.

(39) Y. Yang, Z. Lun, G. Xia, F. Zheng, M. He, Q. Chen, *Energy Environ. Sci.* **2015**, *8*, 3563.

(40) J. Yang, X. Wang, B. Li, L. Ma, L. Shi, Y. Xiong, H. Xu, *Adv. Funct. Mater.* **2017**, *27*, 1606497.

(41) Y. Jia, L. Zhang, A. Du, G. Gao, J. Chen, X. Yan, C. L. Brown, X. Yao, *Adv. Mater.* **2016**, *28*, 9532.

(42) H.-W. Liang, S. Brüller, R. Dong, J. Zhang, X. Feng, K. Müllen, *Nat. Commun.* **2015**, *6*,

7992.

(43) L. Ai, T. Tian, J. Jiang, *ACS Sustain. Chem. Eng*. **2017**, *5*, 4771.

(44) Y. Yang, Z. Lin, S. Gao, J. Su, Z. Lun, G. Xia, J. Chen, R. Zhang, Q. Chen, *ACS Catal.* **2017**, *7*, 469.

(45) Lu, X.; Zhao C. Phys. Chem. Chem. Phys., 2013,15, 20005-20009.

(46) L. T. Qu, Y. Liu, J. B. Baek and L. M. Dai, Acs Nano, 2010, 4, 1321-1326.

(47) Panomsuwan, G.; Saitobcd, N.; Ishizaki, T. J. Mater. Chem. A, 2015,3, 9972-9981.